Prediction of vortex-induced vibration effects on a subsea gravity energy storage module

Novgorodcev, A. R.; Jarquín-Laguna, A.

DOI
10.1201/9781003360773-100

Publication date
2023

Document Version
Final published version

Published in
Trends in Renewable Energies Offshore - Proceedings of the 5th International Conference on Renewable Energies Offshore, RENEW 2022

Citation (APA)
Novgorodcev, A. R., & Jarquín-Laguna, A. (2023). Prediction of vortex-induced vibration effects on a subsea gravity energy storage module. In C. G. Soares (Ed.), *Trends in Renewable Energies Offshore - Proceedings of the 5th International Conference on Renewable Energies Offshore, RENEW 2022* (pp. 907-914). CRC Press / Balkema - Taylor & Francis Group. https://doi.org/10.1201/9781003360773-100

Trends in Renewable Energies Offshore – Guedes Soares (Ed)

Prediction of vortex-induced vibration effects on a subsea gravity energy storage module

A.R. Novgorodcev Jr
Offshore Engineering, Faculty of Civil Engineering and Geosciences, Delft University of Technology, Delft, The Netherlands

A. Jarquín-Laguna
Maritime and Transport Technology, Faculty of Mechanical, Maritime and Materials Engineering, Delft University of Technology, Delft, The Netherlands

ABSTRACT: Subsea buoyancy gravity energy storage systems (SBGESS) could take advantage of large water depth to store energy in the form of potential energy. In the proposed system, drum hoists mounted on a semisubmerged support structure simultaneously lift concrete cylinders with hundreds of tonnes and lower floaters with equivalent buoyancy force, which can be released with high round trip efficiencies by inverting the motor operation. The present study addresses the potential effect of the vortex-induced vibration (VIV) produced by current velocities on the behaviour of the energy storage modules. In order to analyse the system response, a state-of-the-art VIV model was integrated with a spherical pendulum and tuned with experimental results from the literature. The numerical model allows estimating amplitudes and frequencies of oscillation for a single module in both in-line and cross-flow directions. Results are used to assess the risk between modules of collisions on a previously designed SBGESS.

1 INTRODUCTION

Offshore wind energy plays a relevant role in decarbonising the global energy matrix due to this great potential to scale up by 2050 (European Commission 2020). Notably, new technical developments and industrialisation of floating wind turbines will allow the construction of wind energy farms in regions with larger water depths and high-energy potential. Floating Offshore wind could also be used to support the electrification of offshore oil platforms that usually burn up to 5% of their oil and gas production to power their internal processes (Wood Mackenzie 2019). For both grid-connected and autonomous applications, energy storage solutions are required to overcome the intermittent nature of wind resources.

1.1 *Deep water energy storage system*

Wang et al. (2019) presented a review of offshore energy storage technologies. The present work will focus on using potential gravitational energy for applications in the time range of hours to days. Currently, this approach represents 94% of the total energy storage capacity worldwide in the form of Pumped Hydro Storage (PHS). However, only a few concepts are being considered for deep water utilisation.

A promising offshore counterpart of PHS is the gravitational storage system (GES), which utilises submerged weights to store potential energy. Unlike onshore developments with some operating prototypes, limited scientific publications were found on offshore GES. The advantages of this concept are the reported theoretical round-trip efficiencies of up to 85%, the modularity and the relatively low cost per MWh (Saragossi 2018, Wang et al. 2019).

Subsea buoyancy energy storage (ByES) utilises the buoyancy forces to store potential energy, operating similarly to the GES but in the opposite direction. Modelled blocks of floating materials like Styrofoam (Alami 2020) or gas-filled vessels (Bassett et al. 2017) have been proposed to be used as floaters. The theoretical maximum round-trip efficiency for the ByES is reported at 83% (Wang et al. 2019).

Novgorodcev Jr. et al. (2022) proposed an alternative energy storage system that combines buoyancy and gravitational energy storage devices installed in a single semi-submerged support structure, represented in Figure 1. In this schematic, the orange dotted lines represent the power cables, the solid grey the traction cables, and the dashed black the mooring lines. The semi-sub structure is shown in red, and the floaters and weights in blue. This system is called Subsea Buoyancy Gravity Energy Storage System (SBGESS).

DOI: 10.1201/9781003360773-100

The floaters and weights are connected to drum hoists mounted side by side. The hoists will simultaneously retrieve and lift the floaters and weights during the charging process, compensating the resultant vertical forces acting on the support structure. Similarly, the discharge process can occur when the hoist motor is inverted. The resulting neutral vertical force simplifies the system's design requirements by eliminating the need for an active ballasting control to maintain structural stability during operation, which is the case in other offshore GES concepts. Being a semi-submerged platform, the costs to keep a stable position during extreme weather conditions are expected to be lower than free surface floating solutions. The SBGESS is suitable for water depths of at least 1000 m, as the energy storage capacity is proportional to the cables' length.

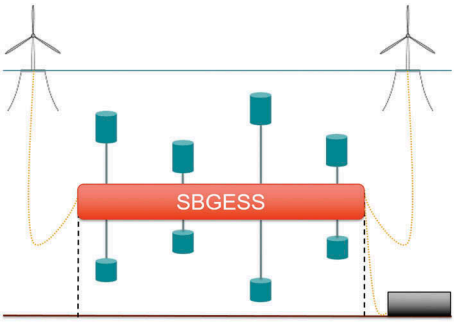

Figure 1. Schematic of the Subsea Buoyancy Gravity Energy Storage System (SBGESS), artistic impression. (Novgorodcev Jr. et al. 2022).

The sea currents at the operation depth are slower than those closer to the surface; nevertheless, they can produce VIV over the weights and floaters, inducing a pendulum motion that could cause collisions between the energy storage components. In the present study, a state-of-the-art VIV model was adapted and integrated with a spherical pendulum as well as validated with available experimental results from the literature. This model was used to estimate the amplitude and frequency of oscillation in both in-line and cross-flow directions as a function of the cable's length and the velocity of sea currents for the energy storage modules presented by Novgorodcev Jr. et al. (2022).

2 VORTEX-INDUCED VIBRATION

VIV is a phenomenon that affects the integrity of multiple engineering structures, from tall buildings and chimneys to small thermocouple pits, passing through submerged oil risers and power cables. Kaneko et al. (2014) presented the history of VIV research and provided a guide to classify and model this phenomenon according to the type of structure and characteristics of the flow. Especial attention was given to modelling the lock-in in the cross-flow direction with semi-empirical models like the Van der Pol wake oscillator and extension of the Morison model. Those models rely on the concept of a wake oscillator that consists of using a non-linear oscillator coupled to the dynamics of a cylinder instead of modelling the entire flow field. Experimental results are used to tune the model parameters. Such phenomenological models give a good estimation of the peak vibration amplitudes but lack accuracy in estimating the critical velocity where lock-in occurs.

Most models do not predict the in-line vibration due to its smaller amplitude compared to those in the cross-flow direction. However, the in-line vibration may introduce further fatigue damage and change the cross-flow response by changing the wake pattern (Qu & Metrikine 2020). To address these effects, some authors have proposed models with an additional uncoupled non-linear oscillator to describe the oscillating drag force. The results of these models show better agreement with experimental results but cannot predict the super-upper branch that appears when the mass ratio (m^*) is reduced below a value of six. This phenomenon, described by Jauvtis & Williamson (2004), consists of a periodic wake with three vortices being formed in each half-cycle (also known as 2T mode), with energy transfer from the in-line to the cross-flow direction by the third vortex, producing amplitudes of around three diameters peak-to-peak.

More recently, Qu & Metrikine (2020) developed a model with only one oscillator coupled to both cross-flow and in-line VIV to better represents the physics as the drag and lift forces have the same origin, even being independent of each other. This model proved better in the prediction of the conventional and the super-upper branch lock-in of an elastically supported rigid cylinder in a cross-flow.

Despite the recent developments, no model in literature was developed to predict the two components of the VIV for a submerged spherical pendulum. This work aims to adapt the model developed by Qu & Metrikine, 2020 with the spherical pendulum motion. Then the model is tuned with the experimental results from Jauvtis & Williamson (2004), using the same mass ratio as the weight of the SBGESS designed by Novgorodcev Jr. et al. (2022). Finally, the tuned model is applied to predict the in-line and cross-flow amplitude and frequency of the weights and floaters of the SBGESS and assess the risk of collision between the proposed energy storage components.

3 MODEL DESCRIPTION

A single gravity element of the SBGESS is modelled as a spherical pendulum fully submerged in water according to the coordinate system proposed by O'Connor & Habibi (2013) and illustrated in Figure 2. The pendulum movement is affected by a constant flow velocity (V) in the X direction, while the gravity is aligned with the Z axis.

In this work, the following assumptions are made: (i) The cable length (L) is constant, it has no flexibility, and it is massless (rigid bar); (ii) the effects of VIV on the cable are neglected; (iii) the pendulums are connected to a fixed position support platform; (iv) the pendulum bob is a perfect cylindrical block considered as a point mass m; (iv) the fluid flow is considered perpendicular to the cylinder, while the cylinder remains aligned with z direction, and the cable is connected at the centre of mass of the cylinder, as represented in Figure 2; (v) the added mass coefficient (C_a), water density (ρ) and viscosity (μ) are constant; (iv) the vertical relative velocity component (U_z) is neglected, so the resulting forces act only in the xy plane;

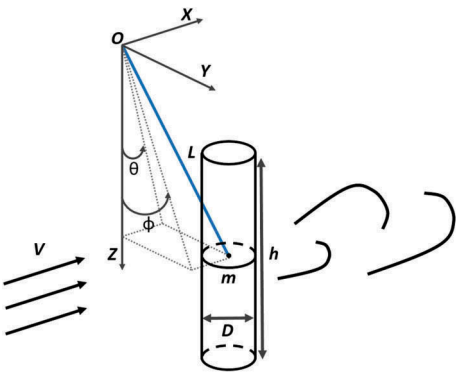

Figure 2. Coupled cross-flow and in-line VIV of a cylindrical pendulum bob subjected to uniform flow.

Following the approach of Qu & Metrikine (2020), the vortex forces that act on the cylinder are decomposed in drag (F_{VD}) and lift (F_{VL}) components which are projected on the cross-flow (F_{VY}) and in-line (F_{VX}) directions as presented in Figure 3. These forces are then projected on the θ and ϕ directions, as represented in Figure 6. This figure also depicts the viscous damping forces ($F_{d\theta}$ and $F_{d\phi}$) that act in the opposite direction to the resulting velocity.

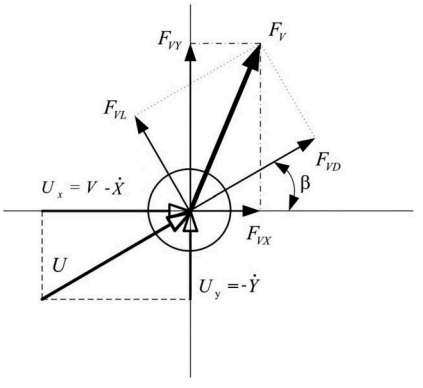

Figure 3. Decomposition of the vortex force in drag, lift, cross-flow and in-line directions (adapted from Ogink & Metrikine (2010)).

3.1 *Kinematic equations*

The equations of motion are derived using the Lagrangian Mechanics approach based on the potential and kinetic energy of the system. The first step is to derive the kinematic equations to describe the pendulum position, as presented below:

$$X = L\sin(\theta), \tag{1}$$

$$Y = L\cos(\theta)\sin(\phi), \tag{2}$$

$$Z = L\cos(\theta)\cos(\phi), \tag{3}$$

with the following resulting velocities:

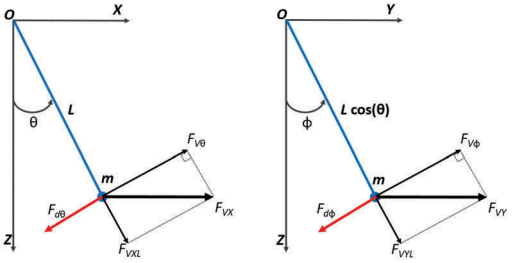

(a) Forces on the XZ plane. (b) Forces on the YZ plane.

Figure 4. Decomposition of the cross-flow and in-line vortex forces in the tangential and radial directions and the representation of the damping force components in θ and ϕ directions.

$$\dot{X} = L\cos(\theta)\dot{\theta}, \tag{4}$$

$$\dot{Y} = -L\sin(\theta)\sin(\phi)\dot{\theta} + L\cos(\theta)\cos(\phi)\dot{\phi}, \tag{5}$$

$$\dot{Z} = -L\sin(\theta)\cos(\phi)\dot{\theta} - L\cos(\theta)\sin(\phi)\dot{\phi}. \tag{6}$$

3.2 *Equations of motion for the spherical pendulum*

The kinetic energy of the spherical pendulum is given by:

$$\begin{aligned} T &= \tfrac{1}{2}m(\dot{Z}^2 + \dot{X}^2 + \dot{Y}^2) \\ &= \tfrac{mL^2}{2}(\dot{\theta}^2 + \cos(\theta)^2\dot{\phi}^2). \end{aligned} \tag{7}$$

The potential energy is:

$$P = mg(L - Z) = mgL(1 - \cos(\theta)\cos(\phi)). \tag{8}$$

So the Lagrangian $\mathscr{L}$ is:

$$\begin{aligned} \mathscr{L} &= T - P \\ &= mL\left(\tfrac{L\dot{\theta}^2}{2} + \cos(\theta)^2\dot{\phi}^2 - g(1 - \cos(\theta)\cos(\phi))\right). \end{aligned} \tag{9}$$

Considering an isotropic damping coefficient b, the Rayleigh dissipation function could be expressed as:

$$\begin{aligned} R &= \tfrac{1}{2} b(\dot{X}^2 + \dot{Y}^2 + \dot{Z}^2) \\ &= \tfrac{bL^2}{2}\left(\dot{\theta}^2 + \cos(\theta)^2 \dot{\phi}^2\right). \end{aligned} \tag{10}$$

As the pendulum has two degrees of freedom (θ and ϕ), the resulting equations of motion are:

$$\frac{d}{dt}\left(\frac{\partial \mathscr{L}}{\partial \dot{\theta}}\right) - \frac{\partial \mathscr{L}}{\partial \theta} + \frac{\partial R}{\partial \dot{\theta}} = \Gamma_\theta, \tag{11}$$

$$\frac{d}{dt}\left(\frac{\partial \mathscr{L}}{\partial \dot{\phi}}\right) - \frac{\partial \mathscr{L}}{\partial \phi} + \frac{\partial R}{\partial \dot{\phi}} = \Gamma_\theta, \tag{12}$$

where Γ_θ and Γ_ϕ are torques caused by external forces in θ and ϕ directions. Substituting Equations 9, 10:

$$\begin{aligned} &mL^2\ddot{\theta} + mL^2\cos(\theta)\sin(\theta)\dot{\phi}^2 \\ &+mgL\sin(\theta)\cos(\phi) + bL^2\dot{\theta} = \Gamma_\theta, \end{aligned} \tag{13}$$

$$\begin{aligned} &mL^2\cos(\theta)^2\ddot{\phi} - 2mL^2\cos(\theta)\sin(\theta)\dot{\theta}\dot{\phi} \\ &+mgL\cos(\theta)\sin(\phi) + bL^2\cos(\theta)^2\dot{\phi} = \Gamma_\phi, \end{aligned} \tag{14}$$

the external torques on the right side can be further decomposed into torque caused by vortex forces ($\Gamma_{V\theta}$ and $\Gamma_{V\phi}$) and by ideal inviscid forces associated with the potential added mass of the fluid ($\Gamma_{A\theta}$ and $\Gamma_{A\phi}$):

$$\Gamma_\theta = \Gamma_{V\theta} + \Gamma_{A\theta} = L\left(F_{VX}\cos(\theta) - m_a L\ddot{\theta}\right), \tag{15}$$

$$\begin{aligned} \Gamma_\phi &= \Gamma_{V\phi} + \Gamma_{A\phi} \\ &= L\cos(\theta)(F_{VY}\cos(\phi) - m_a L\cos(\theta)\ddot{\phi}), \end{aligned} \tag{16}$$

in which the force terms are described as follows:

$$F_{VX} = \frac{1}{2}\rho D h V^2 C_{VX}, \tag{17}$$

$$F_{VY} = \frac{1}{2}\rho D h V^2 C_{VY}, \tag{18}$$

and m_a is the added mass defined as:

$$m_a = \frac{C_a \pi \rho D^2 h}{4}, \tag{19}$$

where C_a is the added mass coefficient, and C_{VX} and C_{VY} are in-line and cross-flow vortex force coefficients, respectively. Replacing the torque terms, rearranging the equation and dividing both sides by their moment of inertia $I_\theta = (m + m_a)L^2$ and $I_\phi = (m + m_a)L^2\cos(\theta)^2$, respectively, the equations of motion become:

$$\begin{aligned} &\ddot{\theta} + 2\zeta\omega_n\dot{\theta} + \sin(\theta)\Big[\omega_n^2\cos(\phi.) \\ &+\left(\tfrac{m^*}{m^*+C_a}\right)\cos(\theta)\dot{\phi}^2\Big] = \tfrac{\Gamma_{V\theta}}{I_\theta}, \end{aligned} \tag{20}$$

$$\begin{aligned} &\ddot{\phi} + 2\zeta\omega_n\dot{\phi} + \tfrac{1}{\cos(\theta)}\Big[\omega_n^2\sin(\phi) \\ &-\left(\tfrac{m^*}{m^*+C_a}2\sin(\theta)\dot{\theta}\dot{\phi}\right)\Big] = \tfrac{\Gamma_{V\phi}}{I_\phi}, \end{aligned} \tag{21}$$

where the natural frequency and the damping ratio of a submerged pendulum are considered $\omega_n = \sqrt{mg/((m+m_a)L)}$ and $\zeta = b/(2\omega_n(m+m_a))$, where m^* is the mass ratio defined as $m^* = \frac{mC_a}{m_a}$.

3.3 *Wake oscillator coupled to both cross-flow and in-line degrees of freedom of the structure*

For the expected sizes of the gravity energy storage unit and the typical current velocities on possible application sites, the reduced velocity, defined as $V_n = \frac{2\pi V}{\omega_n D}$, could be higher than 2.5. For these velocities, the in-line vortexes are shed alternately. According to Qu & Metrikine (2020), the coupling between the in-line motion and the wake variable may be in the form that ensures parametric excitation of the lift force by the in-line vibration. Therefore, the authors derived an extended version of the Van der Pol oscillator equation to include a parametric excitation term presented below:

$$\ddot{q} + \varepsilon\omega_s\left(q^2 - 1\right)\dot{q} + \omega_s^2 q - \frac{\kappa}{D}\ddot{X}q = \frac{A}{D}\ddot{Y}, \tag{22}$$

where q is the wake variable, ε and A are tuning parameters, $\ddot{X}$ and $\ddot{Y}$ could be derived from Equations 4 and 5, and ω_s is the Strouhal frequency defined as $\omega_s = 2\pi StV/D$, in which St denotes the Strouhal number. The wake variable correlates the lifting force (C_{VL}) with the reference lift force measured on a fixed cylinder (C_{L0}), $C_{VL} = 1/2qC_{L0}$. Equation 22 can then be written as:

$$\begin{aligned} &\ddot{q} + \varepsilon\omega_s(q^2-1)\dot{q} + \omega_s^2 q - \tfrac{\kappa L}{D}[-\dot{\theta}^2\sin(\theta) \\ &+\ddot{\theta}\cos(\theta)]q = \tfrac{-AL}{D}[\cos(\theta)\sin(\phi)(\dot{\theta}^2 + \dot{\phi}^2) \\ &+2\sin(\theta)\cos(\phi)\dot{\theta}\dot{\phi} + \sin(\theta)\sin(\phi)\ddot{\theta} \\ &-\cos(\theta)\cos(\phi)\ddot{\phi}]. \end{aligned} \tag{23}$$

3.4 *Dimensionless form of the governing equations*

Considering the definition of the added mass (Equation 19), mass ratio and rewriting V according to the definition of the Strouhal frequency, the right side of the equations of motion (Equations 20, 21) could be written as:

$$\frac{\Gamma_{V\theta}}{I_\theta} = \frac{D\omega_s^2 \cos(\theta) C_{VX}}{2L\pi^3 St^2 (m^* + C_a)}, \tag{24}$$

$$\frac{\Gamma_{V\phi}}{I_\phi} = \frac{D\omega_s^2 \cos(\phi) C_{VY}}{2L\cos(\theta)\pi^3 St^2 (m^* + C_a)}. \tag{25}$$

Replacing these terms and using the following quantities in order to have the equations in dimensionless form:

$$\tau = \omega_s t, \Omega_n = \omega_n/\omega_s, l = L/D, \tag{26}$$

the governing equations become:

$$\theta'' + 2\zeta\Omega_n\theta' + \sin(\theta)\left[\Omega_n^2 \cos\phi + \left(\frac{m^*}{m^* + C_a}\right) cos(\theta)\phi'^2\right] = \frac{\cos(\theta) C_{VX}}{2l\pi^3 St^2 (m * + C_a)} \tag{27}$$

$$\phi'' + 2\zeta\Omega_n\phi' + \tfrac{1}{\cos(\theta)}\left[\Omega_n^2 \sin(\phi) - \left(\tfrac{m^*}{m^* + C_a}\right) 2\sin(\theta)\theta'\phi'\right] = \frac{\cos(\phi) C_{VY}}{2l\cos(\theta)\pi^3 St^2 (m^* + C_a)}, \tag{28}$$

$$q'' + \varepsilon\left(q^2 - 1\right)q' + q - \kappa l[-\sin(\theta)\theta'^2 + \cos(\theta)\theta''] = -Al[\cos(\theta)\sin(\phi)(\theta'^2 + \phi'^2) + 2\sin(\theta)\cos(\phi)\theta'\phi' + \sin(\theta)\sin(\phi)\theta'' - \cos(\theta)\cos(\phi)\phi''], \tag{29}$$

where:

$$C_{VX} = [C_{VL} 2\pi lSt(\sin(\theta)\sin(\phi)\theta' - \cos(\theta)\cos(\phi)\phi') + C_{DM}(1 - 2\pi lSt\cos(\theta)\theta')][(1 - 2\pi lSt\cos(\theta)\theta')^2 + (2\pi lSt)^2(\sin(\theta)\sin(\phi)\theta' - \cos(\theta)\cos(\phi)\phi')^2]^{1/2} + \alpha C_{VL}^2(1 - 2\pi lSt\cos(\theta)\theta')|1 - 2\pi lSt\cos(\theta)\theta'|, \tag{30}$$

$$C_{VY} = [C_{VL}(1 - 2\pi lSt\cos(\theta)\theta') + C_{DM} 2\pi lSt(\sin(\theta)\sin(\phi)\theta' - \cos(\theta)\cos(\phi)\phi')]\left[(1 - 2\pi lSt\cos(\theta)\theta')^2 + (2\pi lSt)^2(\sin(\theta)\sin(\phi)\theta' - \cos(\theta)\cos(\phi)\phi')^2\right]^{1/2}, \tag{31}$$

and $C_{DM} = C_{D0} - 1/2\alpha C_{L0}^2$, where C_{L0} and C_{D0} are the lift force and mean drag coefficients measured on a fixed cylinder. Prime (') represents derivative respect to the dimensionless time τ.

3.5 *Small angle assumption*

Small oscillation angles (θ and $\phi < 0.1$) are expected for this kind of system, so a small angle approach can be adopted. Following this approach, the terms with order higher than two are neglected, and the governing equations become:

$$\theta'' + 2\zeta\Omega_n\theta' + \Omega_n^2\theta = \frac{C_{VX}}{2l\pi^3 St^2 (m^* + C_a)}, \tag{32}$$

$$\phi'' + 2\zeta\Omega_n\phi' + \Omega_n^2\phi = \frac{C_{VY}}{2l\pi^3 St^2 (m^* + C_a)}, \tag{33}$$

$$q'' + \varepsilon\left(q^2 - 1\right)q' + q - \kappa l\theta'' q = Al\phi'', \tag{34}$$

where:

$$C_{VX} = \frac{[C_{VL} 2\pi lSt\phi' + C_{DM}(1 - 2\pi lSt\theta')]}{\sqrt{(1 - 4\pi lSt\theta')} + \alpha C_{VL}^2(1 - 2\pi lSt\theta')|1 - 2\pi lSt\theta'|}, \tag{35}$$

$$C_{VY} = \frac{[C_{VL}(1 - 2\pi lSt\theta') - C_{DM} 2\pi lSt\phi']}{\sqrt{(1 - 4\pi lSt\theta')}}. \tag{36}$$

4 MODEL TUNING

The governing equations (Equations 32, 33, 34) have been implemented and numerically solved on a standard ODE solver to reproduce the experimental results of Jauvtis & Williamson (2004) for $m^* = 2.6$ which is similar to the mass ratio of the weights of the SBGESS if they were made of standard concrete. For this experiment, the cylinder has the same natural frequency in the cross-flow and in-line directions ($f_N = 0.4$) as is expected for the SBGESS components. The dimensionless parameters of the experimental set-up are $C_a = 1$, $\zeta = 0.0036$ and $Re = 2000 - 11000$. For the simulations, the oscillation drag force coefficient of a stationary cylinder ($\alpha C_{L0}^2/2$) is assumed to be 0.1 (with $C_{L0} = 0.3$ and $\alpha = 2.2$), $C_{D0} = 1.2$ and $St = 1.2$.

A sensitivity analysis of the three model tuning parameters (A, ε and κ) was made, and two sets of parameters were selected to reproduce lower and upper response branches separately. For both cases,

$\kappa = 5$, and for the lower branch case (called case L) $A = 22$ and $\varepsilon = 0.7$. For the upper case (called case U) $A = 10$ and $\varepsilon = 0.09$.

Figures 5 and 6 present the dimensionless in-line and cross-flow amplitude responses ($A^* = A/D$). The experiments measured by Jauvtis & Williamson (2004) are depicted as circles, the numerical results from Qu & Metrikine (2020) areas dash-dot lines and the results of the present work as solid lines. The numerical model captured the two in-line amplitude picks at $V_n \approx 2.5$ for both branches, but the second peak amplitude (where vortexes are shred alternately) was captured only for the lower branch. The maximum A_x prediction is half of the experimental measurements, even smaller than the one predicted by Qu & Metrikine (2020). This underprediction could be related to the influence of the cable's length that appears on the right side of the governing equations (Equations 32-36) and on the coupling term of the wake variable ($-\kappa l\theta'' q$) of Equation 34.

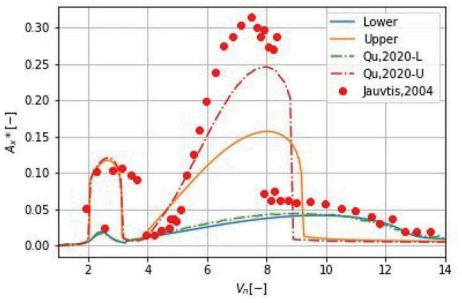

Figure 5. Dimensionless in-line amplitude response as a function of V_n, with m^*=2.6, St=0.2 and C_{D0}=1.2.

The simulations have a good agreement for the cross-flow amplitude response for both lower and upper branches, as shown in Figure 6. The model captured the super-upper branch with the amplitude reaching 1.5D, indicating that it could capture the energy transfer from the in-line to the cross-flow direction.

The normalised cross-flow response frequency is presented in Figure 7, where it is possible to see that the model has captured the initial in-line vibration mode that occurs for $V_n < 4$, characterised by the two single vortices formed per cycle (2S). The model also captured the jump in the vortex phase where the super-upper branch with two triplets of vortices (2T) and higher response amplitude appears. The frequency lock-in remains until $V_n \approx 9$ and 12.5 for the upper and lower branches, respectively, when it increases linearly with V_n. Similar behaviour for the lower branch starts at $V_n \approx 12.5$. At $V_n \approx 1.7$, a peak of $\Omega_Y = \Omega_n$ is caused by the resonance when the third harmonic component in the fluid force approaches the natural frequency of the cylinder

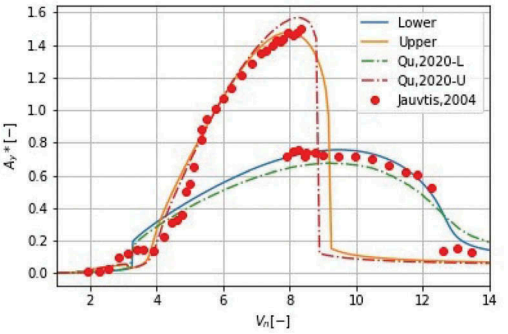

Figure 6. Dimensionless cross-flow amplitude response as a function of V_n, with m^*=2.6, St=0.2 and C_{D0}=1.2.

appears. This peak was also detected by Qu & Metrikine (2020), who concluded that it is not related to lock-in.

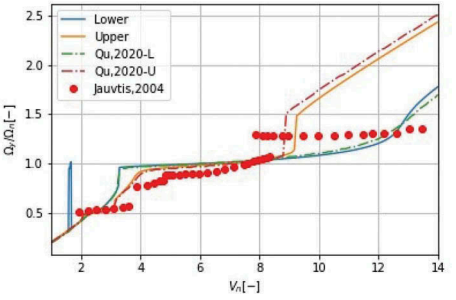

Figure 7. Normalised cross-flow response frequency as a function of V_n, with m^*=2.6, St=0.2 and C_{D0}=1.2.

According to Jauvtis & Williamson (2004), the lower branch characterised by two vortex pairs formed per cycle (2P) starts to exist for $V_n \approx 7.5$, and the upper branch ceases to exist for $V_n \approx 8.5$, with the two modes coexisting in the interval. The present model could not change the modes automatically, but a prediction of the vibration response could be made by knowing that the upper branch should be considered until its amplitude suddenly decreases and the cross-flow frequency gets higher than the natural frequency of the cylinder. From this point, the lower branch could predict the amplitude.

5 CASE STUDY

The tuned model has been applied to assess the amplitude response of stand-alone weight and floater modules of an SBGESS in a real application scenario in the Libra oil field, Brazil. For this application, it is considered that the cable that connects the modules to the main SBGESS structure could be extended between 0 and 1000 m and that the maximum sea current velocity

is $1.3m/s$. The diameter of both systems is 5 meters, and consequently, the maximum expected Reynolds number is 10×10^6, which indicates that the flow is in the supercritical region. The Strouhal number remains constant in this region, but with measured values that vary between 0.22 and 0.29 according to different publications (Schewe 1983), the present study adopts a value of $St = 0.26$. In this region, C_{D0} assumes the value of 0.8. Table 1 presents a summary of the hydrodynamic parameters that were modified from the experimental results for the case study; the remaining parameters are similar to the ones adopted in the previous chapter.

Table 1. Hydrodynamic coefficients.

	m^*	St	C_{D0}
Experimental	2.6	0.2	1.2
Weight	2.6	0.26	0.8
Floater	0.05	0.26	0.8

The cross-flow amplitude response for the weight module is shown in Figure 8. The maximum cross-flow amplitudes response for the upper and lower branches are increased to 1.61 and 0.99 and reached at smaller values of V_n 5.8 and 7.6. This behaviour was expected for higher Strouhal numbers, which indicates that a higher vortex shedding frequency is expected for the same cross-flow velocity and for a lower mean drag coefficient which leads to smaller energy dissipation and consequently to higher oscillation amplitudes. The maximum in-line amplitude has an opposite behaviour, with values of 0.16 and 0.04 for the upper and lower branches, indicating that more energy is being transferred to the cross-flow due to the smaller drag coefficient that implies smaller forces imposed by the fluid in the cross-flow direction.

In the case of the floater, the expected increase in the cross-flow amplitude response caused by the smaller m^* is counteracted with the reduction caused by the higher St number and smaller C_{D0}, resulting in a smaller maximum value of 1.51 but with a similar peak position with the validation case, as can be seen in Figure 9. The shapes of the curves present smoother growth until the maximum value, without an abrupt drop after that point. The upper branch also exhibits a new increase from $V_n > 11.6$, reaching a maximum value at $V_n = 17.3$, when it starts to decrease very slowly. Qu & Metrikine (2020) showed that the peak amplitude of the upper branch increases with m^* for a constant $(m^* + C_a)\zeta$; however, not in a linear manner. Govardhan & Williamson (2000), on the other hand, showed in one degree of freedom experiments that for $m* < 0.54$, the frequency of the lower branch tends to infinity, ceasing its existence, while the upper branch amplitude keeps the peak amplitude with the increase of V_n. This behaviour was not observed in the present

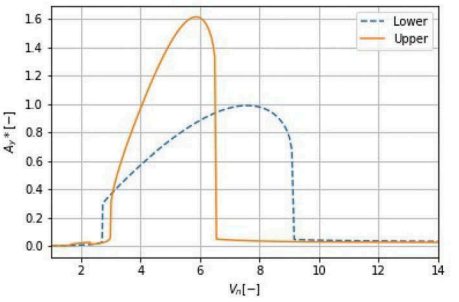

Figure 8. Weight dimensionless cross-flow amplitude response as a function of V_n, with m^*=2.6, St=0.26 and C_{D0}=0.8.

work, but it is important to mention that in this experimental set-up, the cylinder could not move in the in-line direction and that the addition of the second degree of freedom could significantly influence the overall behaviour. To the authors' knowledge, experimental results for $m^* < 0.54$ and two degrees of freedom are not available in the literature, so additional studies are required to adjust the model in this regime.

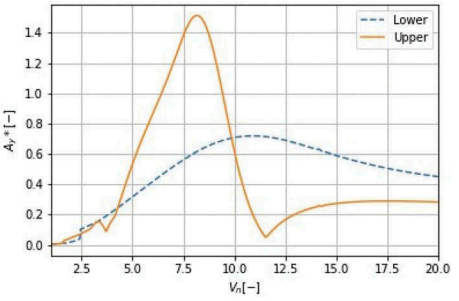

Figure 9. Floater dimensionless cross-flow amplitude response as a function of V_n, with m^*=0.05, St=0.26 and C_{D0}=0.8.

As the cross-flow amplitude showed bigger values than the in-line, they will be used as the reference for assessing the risk of collision between the energy storage components of the SBGESS. In the preliminary design proposed by Novgorodcev Jr. et al. (2022), the distance between the elements is equivalent to one diameter. Thus, any amplitude larger than 0.5 represents a real risk of collision. Such limit is exceeded by the weight for $3.21 < V_N < 6.56$ and for the floaters for $4.9 < V_N < 10.28$. For the weights, collisions could occur for three conditions: (i) current speeds between 0.3 and 1 m/s and cable lengths higher than 75 m; (ii) speeds between 1 and 1.3 m/s and lengths from 50 to 100 m; (iii) higher speeds with cable lengths smaller than 75 m. For the floaters, no collisions are predicted for speeds higher than 0.6 but could occur for cable lengths higher than 300 and speeds as low as 0.1 m/s.

These restrictive operational windows show that the design needs to be revised to increase the distance between the modules or to add active or passive vibration damping to the components. It is also essential to note that the methodology proposed in the present work did not consider any interaction between the energy storage modules, such as the synchronisation effect that could influence the minimal distance required. The proximity effect was also not considered, which could require even a higher distance.

6 CONCLUSION

A state-of-the-art VIV model initially developed and validated to predict the dynamic behaviour of an elastically mounted cylinder in a cross-flow was integrated with a spherical pendulum and tuned with experimental results. The new model has good agreement with the experimental data for cross-flow amplitude and frequency, able to predict the super-upper branch phenomena. The model under-predicted the maximum in-line amplitude for the higher branch, which could be partially attributed to the influence of the cable length in the equations of motion of the spherical pendulum.

The proposed model was then applied to assess the amplitude response of stand-alone gravity and buoyancy energy storage models of an SBGESS. The simulation results indicate that some combinations of cable length and current speed could lead to potential collisions between the energy storage modules. The distance between the modules could be increased, or vibration dampers could be adopted to mitigate this risk.

The developed model could also be applied to evaluate the dynamic behaviour of submerged, lifted weights with m* higher than 0.54, which corresponds to a wide range of industrial applications. New experimental results for very low m* cylinders with two degrees of freedom are required to further develop the model for floater applications. Further works will include the interaction of multiple modules installed on movable platforms and consider the proximity effects.

ACKNOWLEDGEMENTS

The authors would like to thank PETROBRAS, Brazil, for supporting this work.

REFERENCES

Alami, A. H. (2020). “Buoyancy Work Energy Storage (BAES) Systems”. In: *Mechanical Energy Storage for Renewable and Sustainable Energy Resources*. Cham, Switzerland: Springer, pp. 87–92. ISBN: 978-3-030-33788-9. 10.1007/978-3-030-33788-9_2.

Bassett, K. P., Carriveau, R. & Ting, D. S. (2017). “Integration of buoyancy-based energy storage with utility scale wind energy generation”. In: *Journal of Energy Storage* 14, pp. 256–263. ISSN: 2352152X. URL: https://doi.org/10.1016/j.est.2017.04.013.

European Commission (2020). *An EU Strategy to harness the potential of offshore renewable energy for a climate neutral future*. Tech. rep. Brussels.

Govardhan, R. &Williamson, C. H. K. (2000). “Modes of vortex formation and frequency response of a freely vibrating cylinder”. In: *Journal of Fluid Mechanics* 420, pp. 85–130.

Jauvtis, N. & Williamson, C. H. K. (2004). “The effect of two degrees of freedom on vortex-induced vibration at low mass and damping”. In: *J. Fluid Mech*. 509, pp. 23–62.

Kaneko, S., Nakamura, T., Inada, F., Kato, M., Ishihara, K., Nishihara, T., Murethi, N. W. & Langthjem, M. A. (2014). “Vibration Induced by Cross-Flow”. In: *Flow-Induced Vibrations Classifications and Lessons from Practical Experiences Vibrations Classifications and Lessons*. Elsevier. Chap. 2, pp. 29–115.

Novgorodcev Jr., A. R., Mols, F. & Jarquin Laguína, A. (2022). “Subsea buoyancy and gravity energy storage system for deep-water applications: a preliminary assessment”. In: *Proceedings of the ASME 2022 41st International Conference on Ocean, Offshore and Arctic Engineering - OMAE 2022*. Hamburg, Germany.

O’Connor, W. & Habibi, H. (2013). “Gantry crane control of a double-pendulum, distributed-mass load, using mechanical wave concepts”. In: *Mechanical Sciences* 4.2, pp. 251–261. ISSN: 2191916X.

Ogink, R. H. & Metrikine, A. V. (2010). “A wake oscillator with frequency dependent coupling for the modeling of vortex-induced vibration”. In: *Journal of Sound and Vibration* 329.26, pp. 5452–5473. ISSN: 0022460X. URL: http://dx.doi.org/10.1016/j.jsv.2010.07.008.

Qu, Y. & Metrikine, A. V. (2020). “A single van der pol-wake oscillator model for coupled cross-flow and in-line vortex-induced vibrations”. In: *Ocean Engineering* 196. October 2019, p. 106732. ISSN: 00298018.

Saragossi, R. (2018). *Sink Float Solutions: Assessing the feasibility of an energy storage solution*. Tech. rep. ENGIBEX,p. 7. URL: engibex.com.

Schewe, G. (1983). “On the force fluctuations acting on a circular cylinder in crossflow from subcritical up to transcritical Reynolds numbers”. In: *Journal of Fluid Mechanics* 133, pp. 265–285.

Wang, Z., Carriveau, R., Ting, D. S.-K., Xiong, W. & Wang, Z. (2019). “A review of marine renewable energy storage”. In: *International Journal of Energy Research* 43, pp. 6108–6150.

Wood Mackenzie (2019). *Why powering oil and gas platforms with renewables makes sense*. Tech. rep. October.